

Impact Forces and Energy of Flow-like Landslides Against Protection Barriers: a New MPM-validated Empirical Formulation

Angela Di Perna

University of Salerno: Universita degli Studi di Salerno

Sabatino Cuomo (✉ scuomo@unisa.it)

Universita degli Studi di Salerno <https://orcid.org/0000-0001-8024-0319>

Mario Martinelli

Deltares and Technical University of Delft

Research Article

Keywords: impact mechanisms, mitigation, structure, Material Point Method

Posted Date: January 3rd, 2022

DOI: <https://doi.org/10.21203/rs.3.rs-1197305/v1>

License:  This work is licensed under a Creative Commons Attribution 4.0 International License.

[Read Full License](#)

Impact forces and energy of flow-like landslides against protection barriers: a new MPM-validated empirical formulation

Angela Di Perna*, Sabatino Cuomo*, Mario Martinelli^{^,^^}

* University of Salerno, Italy

[^] Deltares, Delft, Netherlands

^{^^} Technical University of Delft, Netherlands

Abstract

Full understanding the interaction mechanisms between flow-like landslides and the impacted protection structures is an open issue. In fact, while researchers have used several approaches, from experimental to numerical, it is true that the adequate assessment of the hydromechanical behaviour of the landslide body requires both a multiphase and large deformation approach.

This paper firstly proposes a conceptual framework for a specific type of protection structure, namely a rigid barrier fixed to the base ground. Two different approaches are proposed: i) an advanced hydro-mechanical numerical model based on Material Point Method is tested in simulating the whole complex landslide-structure-interaction mechanism(s), ii) a more simplified empirical model is casted to estimate the impact force and the time evolution of kinetic energy. The calibration and validation of the empirical formulation are pursued, respectively, based on the MPM numerical results, and referring to a large dataset of field evidence for the peak impact pressure. Finally, the performance of the newly proposed empirical method is compared to the methods available in the literature and its advantages are outlined.

Keywords: impact mechanisms, mitigation, structure, Material Point Method

List of abbreviations

a_1 (–)	coefficient of the power law
a_2 (–)	coefficient of the power law
\mathbf{a}_L (m/s^2)	liquid acceleration
\mathbf{a}_S (m/s^2)	solid acceleration
B (m)	greater base of the barrier
b (m)	smaller base of the barrier
\mathbf{b} (kPa)	body force vector
c' (kPa)	effective cohesion
d (m)	distance between landslide and barrier
\mathbf{D} (kPa)	tangent stiffness matrix
dp_L (kPa)	excess pore pressure
$d\sigma'$ (kPa)	increment of effective stress
E (kPa)	Young modulus of soil
$E_{k,1}$ (kJ)	kinetic energy of the landslide

44	F_1 (kN/m)	contact force along the base of the flow
45	F_2 (kN/m)	impact force along the side of the barrier
46	F_3 (kN/m)	contact force along the smaller base of the barrier
47	$F_{peak,dyn}$ (kN/m)	dynamic peak impact force
48	$F_{peak,stat}$ (kN/m)	static peak impact force
49	Fr (–)	Froude number
50	f_d (kPa)	drag force vector
51	g (m/s ²)	gravity vector
52	k (m ²)	intrinsic permeability
53	k_{sat} (m/s)	saturated hydraulic conductivity
54	K_L (kPa)	elastic bulk modulus of the liquid
55	h (m)	flow height
56	H (m)	barrier height
57	LSI	Landslide-Structure-Interaction
58	L_1 (m)	flow length
59	L_2 (m)	length of barrier's lateral side
60	MPM	Material Point Method
61	m_1 (kg)	landslide mass
62	n (–)	porosity
63	p_L (kPa)	liquid pressure
64	t (s)	time
65	t_0 (s)	initial reference time
66	t_{imp} (s)	time related to LSI beginning
67	t_f (s)	final time of LSI
68	T_1 (s)	time related to the peak impact force
69	T_2 (s)	final time of impact phase
70	V_1 (m ³)	volume of the mixture
71	$V_{f,HL}$ (m ³)	volume retained by the barrier
72	V_L (m ³)	liquid phase volume
73	V_S (m ³)	solid phase volume
74	\mathbf{v}_L (m/s)	liquid velocity vector
75	\mathbf{v}_S (m/s)	solid velocity vector
76	\mathbf{v}_1 (m/s)	landslide velocity
77	x (m)	horizontal Cartesian coordinate
78	y (m)	vertical Cartesian coordinate
79	α (–)	dynamic impact coefficient
80	τ (–)	ratio between T_1 and T_2
81	β (°)	angle between lateral side and base of the barrier
82	$\Delta a_{S,contact}$	change in solid phase acceleration induced by the contact formulation
83	$\Delta a_{L,contact}$	change in liquid phase acceleration induced by the contact formulation
84	Δt_{cr} (–)	critical time step
85	δ (°)	contact friction angle between flow and barrier
86	$\boldsymbol{\varepsilon}$ (–)	strain vector
87	κ (–)	static impact coefficient
88	μ_L (kPa · s)	liquid dynamic viscosity
89	ν (–)	Poisson's ratio
90	ρ_L (kg/m ³)	liquid density
91	ρ_m (kg/m ³)	density of the mixture
92	ρ_S (kg/m ³)	solid density
93	$\boldsymbol{\sigma}$ (kPa)	total stress tensor of the mixture
94	$\dot{\boldsymbol{\sigma}}$ (kPa/s)	Jaumann stress rate matrix
95	$\boldsymbol{\sigma}_n$ (kPa)	normal stress
96	φ' (°)	internal friction angle
97	ψ (°)	dilatancy angle

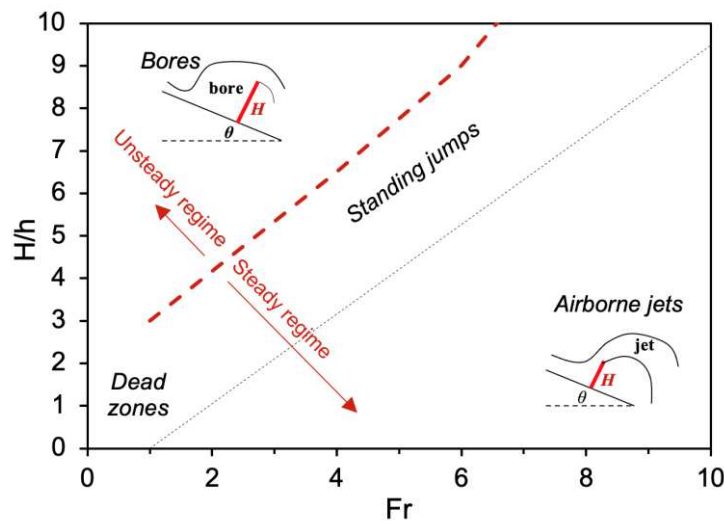
98 1 Introduction

99

100 The interaction of flow-like landslides with rigid walls, obstacles, protection structures and, more
101 recently, single building or cluster of buildings have been investigated by a variety of numerical tools.
102 The massive use of numerical methods is related to the inner complexity of Landslide-Structure-
103 Interaction (LSI) mechanisms, which are related to: i) the hydro-mechanical features of the impacting
104 flow, ii) the geometry of the structure, and iii) initial and boundary conditions for the specific LSI
105 problem. Applications of Discrete Element Method (DEM) has been reported by Leonardi et al.
106 (2016), Calvetti et al. (2017) and Shen et al. (2018). However, a number of continuum mechanics
107 models based on Eulerian methods (Moriguchi et al. 2009), Lagrangian particle-based methods such
108 as Smoothed-Particle Hydrodynamics (SPH), Particle Finite Element Method (PFEM), Finite
109 Element Method with Lagrangian integration points (FEM-LIP), Material Point Method (MPM),
110 (Idelsohn et al. 2006; Bui and Fukagawa 2013; Cuomo et al. 2013; Ceccato et al., 2018) have been
111 also applied. Some coupled Eulerian-Lagrangian methods (Qiu et al. 2011; Jeong et al. 2019) have
112 been also used. Recently the solid-fluid hydro-mechanical coupling and the role of the interstitial fluid
113 in the LSI mechanisms have been considered. For instance, the impact behaviour of saturated flows
114 against rigid barriers was simulated through MPM analyses, with a satisfactory correspondence with
115 the experimental centrifuge test results (Cuomo et al., 2021). Most of these approaches are very
116 recent, and still need comprehensive validation combined with more efforts to reduce the
117 computational cost, which is very high once realistic simulations are pursued.

118 A more traditional approach is based on: i) direct observation of impact of flow-like landslides
119 against barriers, and ii) correlation of the achieved measurements.

120 The measurements available in the literature have been mostly obtained in reduced-scale flume
121 tests (Hübl et al., 2009; Armanini et al., 2011; Canelli et al., 2012; Ashwood and Hungr, 2016; Vagnon
122 and Segalini, 2016), or in some cases in full-scale flume experiments (De Natale et al., 1999;
123 Bugnion et al., 2012). For instance, the interpretation of a wide set of reduced-scale laboratory
124 experiments on dry granular flows allowed Faug (2015) to propose a so-called phase-diagram based
125 on (i) Froude number (Fr) and (ii) obstacle height relative to the flow depth (H/h). The diagram
126 comprises four *LSI* mechanisms: a) Dead zone (i.e. gradual accumulation of material behind the
127 obstacle): this is the case of relatively slow flows ($Fr < \approx 1$) impacting relatively small obstacles
128 ($H/h \approx 1$); b) Airborne jet (forming downstream of the obstacle): this stands for rapid flow ($Fr \gg 1$)
129 and obstacle height low; c) Standing jumps (propagating downstream of the obstacle with steady-
130 state conditions): for rapid flow ($Fr \gg 1$); d) Bores (a granular jump hits the obstacle and propagates
131 upstream of it): in the case of a rapid flow ($Fr \gg 1$) hitting a wall spanning the entire width of the flow
132 ($H/h \gg 1$) with unsteady conditions. However, the interstitial water may largely contribute to
133 change/regulate the landslide-structure interaction mechanism(s), and new insights will be proposed
134 in this paper.



136
137 *Figure 1. Interaction diagram for a flow impacting an obstacle (adapted from Faug, 2015)*
138

136

137

138

139

140

141

142

143

144

145

146

147

148

149

150

151

152

153

154

155

156

157

158

159

160

161

In general, the reduced-scale laboratory tests have been extensively used to derive and validate the empirical formulations most commonly used to assess the peak impact pressure in the design of protection measures against landslide (Schild et al., 2013; Scotton and Deganutti, 1997; Arattano and Franzi 2003; Hübl et al., 2009; Proske et al., 2011; Bugnion et al. 2012; Canelli et al. 2012; He et al. 2016; Song et al., 2021). The existing empirical methods can be classified into three groups: (i) hydro-static methods, which require only flow density and thickness for evaluating the maximum impact pressure; (ii) hydro-dynamic methods, based on flow density and the square velocity of the flow; (iii) mixed methods, that accounts for both the static and the dynamic components of the flow. The weak point is that the empirical formulations greatly depend on empirical coefficients which are difficult to estimate in the practical applications due to their wide range of variation. Common to those approaches are the following assumptions: (i) the impact load is assumed to be totally transferred to the structure without any dissipation during the impact, and (ii) the size, stiffness and inertial resistance of the artificial barrier are not considered (Vagnon and Segalini, 2016). These assumptions generally lead to safe assessment of the peak impact force but with large overestimation of the barrier design. Hence, enhancements will be proposed in this paper on both these topics.

The present work investigates the impact mechanisms of flow-like landslides against artificial barriers in full-scale realistic scenarios. A Conceptual Model of Landslide-Structure-Interaction (LSI) is firstly proposed. Then, two methods are evaluated in this paper: (i) a Material Point Method approach is used to analyse the hydro-mechanical interaction of saturated flows with different types of barriers, (ii) an empirical method is casted to evaluate the peak impact horizontal force and reduction in kinetic energy of the flow. The new empirical formulation is calibrated with a set of numerical MPM results and validated with a large dataset of field evidence of impact problems. Then,

162 the novel empirical formulation is compared with those from the literature and its potential and
163 limitations are discussed.

164

165 **2 A conceptual framework for Landslide-Structure-Interaction (LSI)**

166

167 The proposed conceptual model for Landslide-Structure-Interaction (*LSI*) considers a flow-like
168 landslide mass that impacts against a barrier fixed to the base ground (Fig. 2). The landslide body
169 has the following features: unitary width, length L_1 , depth h , density of the mixture ρ_m , initial uniform
170 velocity $v_{1,0}$, pore-water pressure p_L and friction angle along the base ground equal to $\tan \varphi_b$. The
171 barrier is typically represented by a reinforced concrete vertical wall or by an embankment with a
172 steep inclined face at the impact side. For the sake of generality, here below we consider that the
173 barrier is trapezoidal shaped, with the geometric characteristics being as follows: greater base
174 B , smaller base b , height H , inclination of the impacted side β .

175 The *LSI* problem is described through the following timelines: initial configuration (t_0), landslide
176 propagation ($t_0 < t < t_{imp}$), impact of the landslide front (t_{imp}), time of the peak impact force (T_1),
177 start of the inertial stage (T_2), end of *LSI* (t_f). Before the landslide reaches the barrier ($t_0 < t < t_{imp}$),
178 i.e., during the propagation stage, the *LSI* problem is governed by the basal frictional force F_1 (Eq.
179 1), which acts along the bottom of the flow (L_1) and controls the reduction in flow velocity, resulting
180 in a decrease of the impact forces. Once the flow starts to interact with the barrier ($t_{imp} < t < T_2$),
181 additional stresses (mostly orthogonal to the impacted surface, hence horizontal in many
182 applications) are produced at the impacted side of the barrier. Many studies (e.g., Cui et al., 2015;
183 Song et al. 2017) demonstrated that the total impact force-time history can be simplified as a
184 triangular force impulse, usually with a rise time (T_1) much shorter than the decay time ($T_2 - T_1$).

185 According to the Newton's Third law of motion, the mutual impact forces (F_2) between the
186 landslide and the barrier are equal and opposite. Such mutual stress makes: (i) the flow to decelerate
187 and (ii) the barrier to slip along the base and to deform itself, as shown in Fig. 2. The evaluation of
188 the impact forces applied on the inclined side of the barrier (L_2) is fundamental to design the
189 structural characteristics of the barrier (Eq. 2). It is worth noting that the flow may overtop the barrier
190 during the impact, generating an additional force F_3 on the structure (Eq. 3), mainly dependent on
191 the flow-barrier frictional contact ($\tan \delta$).

192 Once the action F_1 , F_2 and F_3 are known, the stability of the barrier can be determined through
193 the evaluation of the constraint reactions by solving the equilibrium of forces and moments. In this
194 way, it is possible to assess the ultimate strength to which the foundation systems must be designed,
195 or to understand what resistance must be mobilized at the base, so that the barrier does not move.
196 The latter option can be put into practice by placing a layer of soil material suitable to give an
197 assigned frictional resistance to the base of the barrier.

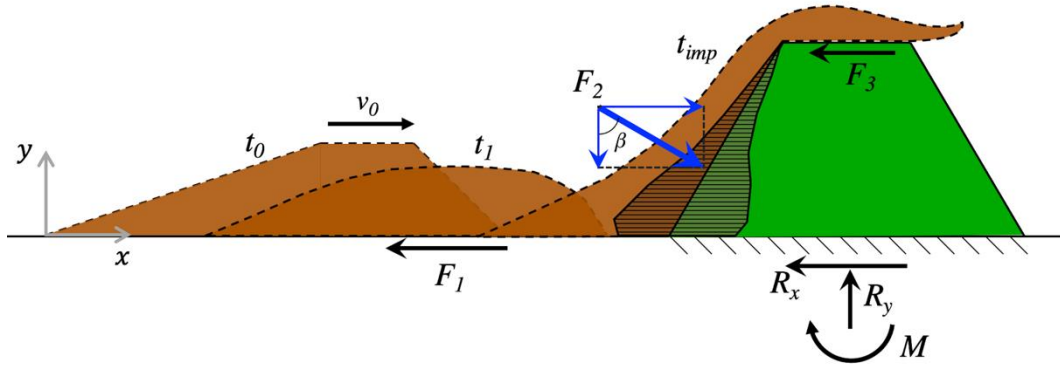
198

$$F_1(t) = \int_0^{L_1(t)} (\rho_m - \rho_L) gh(x, t) \tan \varphi_b dx \quad (1)$$

$$F_2(t) = \int_0^{L_2} (\rho_m - \rho_L) a(t) h(x, t) dx + \int_0^{L_2} p_L(x, t) dx \quad (2)$$

$$F_3(t) = \int_0^b (\rho_m - \rho_L) gh(x, t) \tan \delta dx \quad (3)$$

202



203

204 *Figure 2. Conceptual scheme for Landslide-Structure-Interaction (LSI)*

205

206 **3 MPM parametric analysis of Landslide-Structure-Interaction (LSI)**

207

208 **3.1 Governing equations and input data**

209

210 It is quite difficult to propose a standard landslide configuration as initial condition since it must
 211 represent the shape of the flow in a certain moment of its propagation stage. As known, this
 212 configuration strongly depends on the flow-path topography and on the geomorphological conditions
 213 that can vary from site to site. However, many studies have demonstrated that the front is often
 214 higher than the rear portion due to friction with the ground topography (Iverson, 1997; Thouret et al.,
 215 2020). For this reason, the chosen initial configuration of the landslide is characterized by a 45°-
 216 inclined front and a tail of length equal to three times the flow height. To consider different flow
 217 volumes, an i number of squares have been placed between the head and tail portions. Given this
 218 shape, the landslide as the same volume of an equivalent rectangular with the same height h and a
 219 length $L_m = (2 + i) \cdot h$, and unitary width (Fig. 3).

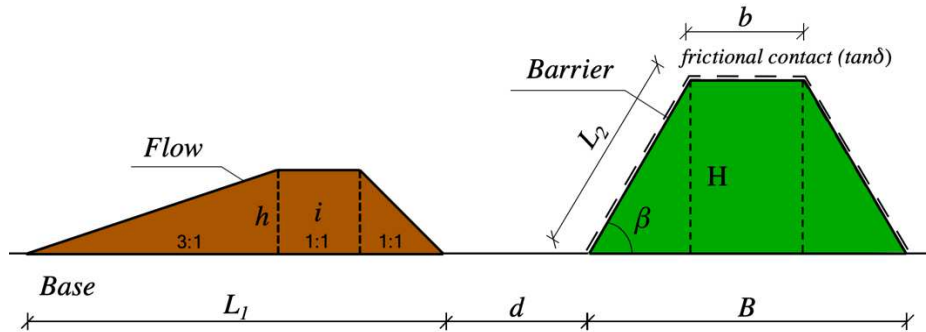
220 The flow and barrier are modelled through the single-point MPM formulation, respectively with 2-
 221 phase and 1-phase, both described in the Appendix 1. For the barrier it is assumed: non-porous
 222 material, the base fixed to the ground and rigid behaviour. This last hypothesis relates to the
 223 construction mode typically used for such barriers (Cuomo et al., 2019). To schematize the problem

224 in a realistic way, the build-up of excess pore pressure in the flow material during the impact is
 225 considered as well as the hydro-mechanical coupled behaviour and the yielding of the flow material.

226 The influence of different impact scenarios on the dynamics and kinematics in a *LSI* problem have
 227 been investigated. The geometric features of both the landslide and the barrier are summarized in
 228 Table 1. It is worth noting that the case of an infinite wall is that considered in the literature empirical
 229 models. The mechanical properties of the saturated flow mass and the friction angle at the contact
 230 with the barrier are reported in Table 2. The numerical MPM analyses evidently allow the
 231 simultaneous simulation of flow propagation and flow-structure interaction. The flow is a saturated
 232 mixture with hydrostatic distribution of initial pore-water pressure. Although simplified, the landslide
 233 scheme resembles its main characteristics such as velocity, impact height, non-zero interstitial
 234 pressures and elasto-plastic behavior. The computational unstructured mesh is made of 20,515
 235 triangular 3-noded elements with dimensions ranging from 0.20 to 1.00 m. The landslide is assumed
 236 as approaching the barrier with a fixed geometric configuration and constant velocity, until LSI starts.

237 The phase diagram proposed by Faug (2015) for granular flow-structure interaction is here used
 238 here to predict the type of impact mechanism expected for each scenario (Table 3). The Froude
 239 number is here calculated as $v_0 \sin \beta / \sqrt{gh}$, considering the inclination β of the impacted side of the
 240 barrier. For practical applications, this could be useful to preliminary assess the potential efficiency
 241 of the barrier in intercepting the propagation of the flow under different impact conditions.

242



243

244

Figure 3. Geometric schematization of the problem in the numerical model

245

246

Table 1. Geometric features for different scenarios

ID	L_1 (m)	L_m (m)	i (-)	h (m)	V_1 (m^3/m)	$v_{0,1}$ (m/s)	β ($^\circ$)	d (m)	L_2 (m)	B (m)	b (m)	H (m)
1	21.00	15.00	3	3.00	45.00	10	60	3.00	6.95	11.00	4.00	6.00
2	21.00	15.00	3	3.00	45.00	20	60	3.00	6.95	11.00	4.00	6.00
3	21.00	15.00	3	3.00	45.00	10	90	3.00	∞	-	-	∞
4	47.00	45.00	43	1.00	45.00	10	60	3.00	6.95	11.00	4.00	6.00

247

248

Table 2. Mechanical properties

Flow-like landslide											Barrier	
ρ_m (kg/m^3)	ρ_s (kg/m^3)	n (-)	K_0 (-)	φ' ($^\circ$)	c' (kPa)	E' (MPa)	ν (-)	k_{sat} (m/s)	μ_L ($Pa s$)	K_L (MPa)	ρ (kg/m^3)	$\tan(\delta)$ (-)
1800	1300	0.5	0.66	20	0	2	0.25	10^{-4}	10^{-3}	30	2000	0.29

249

250

Table 3. Expected impact mechanism

ID	Fr (-)	H/h (-)	Impact mechanism*
1	1.59	2.0	Standing jump
2	3.19	2.0	Airborne jets
3	1.84	∞	Bores
4	2.76	6	Bores

* from the application of the diagram proposed by Faug (2015)

251

252 3.2 Numerical MPM results

253

254 Selected results are shown in Figures 4-5, where the spatial distribution of pore-water pressure
 255 is illustrated at different time instants of the propagation stage for all scenarios of Table 1. During
 256 the impact, the initial liquid pressure ($< 30 kPa$) changes over time, with the maximum value in the
 257 first instants of the impact process ($t = 1 s$) and later diminishing down to nil in some cases.
 258 However, the maximum value of pore water pressure ($p_{L,max}$) is dependent on the type of barrier. In
 259 fact, comparing an infinite wall (Fig. 4a) with a fixed artificial barrier (Fig. 4b), it follows that $p_{L,max}$ is
 260 higher in the first case, where the overtopping is not allowed and the impacted area of the barrier is
 261 larger than for the artificial barrier ($t = 1 s$). At $t = 2 s$, the flow overtops the wall (Fig. 4a) or goes
 262 beyond the barrier forming a prolonged jet (Fig. 4b). Liquid pressure is decreasing, indicating that
 263 we are in the decay zone of the impact force diagram. Subsequently ($4 s < t < 6 s$), the flow loses
 264 more and more energy and falls downwards (similarly, in both cases). The expected impact
 265 mechanism, as assessed from the use of the diagram by Faug (2015), is confirmed in both the cases.
 266 For the infinite vertical wall, the impact mechanism resembles the bores regime since a granular
 267 jump (named "bore") is formed which heads upstream of the wall. For the embankment barrier, the
 268 impact mechanism is the standing jump, which is similar to the bores regime but here a part of the
 269 incoming flow is able to overtop the barrier, forming a jet with very low energy.

270 Different flows are also considered to investigate other impact mechanisms (Fig. 5). High flow
 271 velocities induce large values of $p_{L,max}$, which reaches 260 kPa (Fig. 5a). In this case, the expected
 272 impact mechanism is an airborne jet (Table 3) and it is confirmed very well from the numerical

273 simulation. A very prolonged jet with high energy is formed after the impact, thus the amount of
274 material that is retained by the barrier is much smaller than the standing jump case. Completely
275 different is the case of a shallow flow (Fig. 5b), where the flow hits the obstacle and propagates
276 upstream in unsteady conditions (bores regime). The flow has a very low reduction in kinetic energy,
277 however the flow does not overtop the barrier.

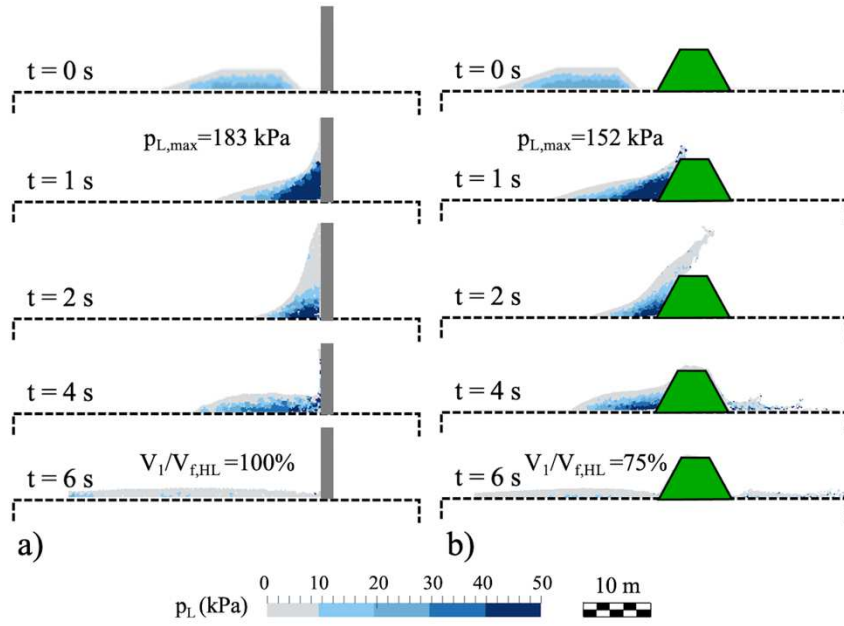
278 Overall, the cases 1, 2 and 4 suggest a clear link between pore-water pressures at impact and
279 the amount of overtopping flow mass, where larger pore-water pressures facilitate the overtopping
280 of the barrier. This finding is also confirmed by previous experimental research (Song et al., 2017;
281 Zhou et al., 2018).

282 Fig. 6 shows the landslide-structure interaction from both a dynamic and kinematic point of view.
283 The peak of the horizontal and vertical components of the impact force ($F_{2,x}$ and $F_{2,y}$, respectively in
284 Fig. 6a) are quite different in all cases. In particular, the forces have a clear peak for case 1, 2 and
285 3, with higher values as the velocity increases and as the impacted side gets steeper. Conversely,
286 case 4 does not show any distinct peak, where the impact forces are very limited.

287 The temporal variation of the forces F_3 and F_4 (defined in Fig. 2) are also illustrated in Fig. 6b.
288 The frictional force above the barrier (F_3) is caused by the overtopping volume. In fact, the highest
289 value is in case 2, where the retained volume is the smallest. This force can also have a negative
290 sign when the flow goes upstream, instead of flowing beyond the barrier. However, for what concerns
291 the global momentum balance of the barrier, the contribution of F_3 is negligible compared to the
292 frictional force at the base of the barrier F_4 .

293 For the sake of simplicity, the flow basal frictional force F_1 is assumed equal to zero in all cases,
294 by means of a smooth contact.

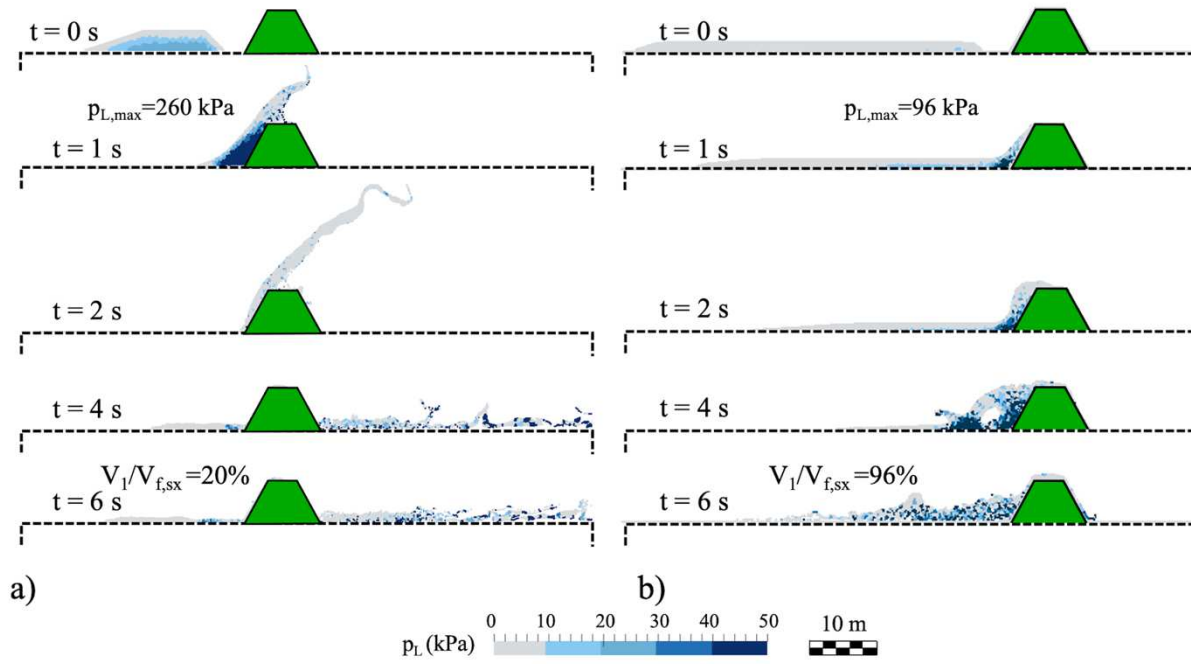
295 The kinetic energy of the incoming flow (E_{k1}) is plotted in Fig. 6. In order to make a more
296 comprehensive comparison, the curves are normalized by the initial kinetic energy of the flow ($E_{k1,0}$).
297 The curves of cases 1, 2 and 3 show a sudden reduction, reaching the minimum value at
298 approximately $t \cong 2 s$ and, after that, the energy increases again as the formed jet takes the
299 downward direction. This means that, during the flow, the kinetic energy is transformed to potential
300 energy. In particular, for $t > 2 s$ all the trends are very different, since the curves represent the kinetic
301 energy of the overcoming jet (especially for cases 1 and 2) combined with the energy of the reflecting
302 flow (especially for case 3). The behavior of case 4 is completely different: it is characterized by a
303 slower and constant reduction of the energy as the impact mechanism does not induce the formation
304 of any jet.



305

306

Figure 4. Pore-water pressure distribution for: (a) infinite wall (case 3); (b) artificial barrier (case 1)

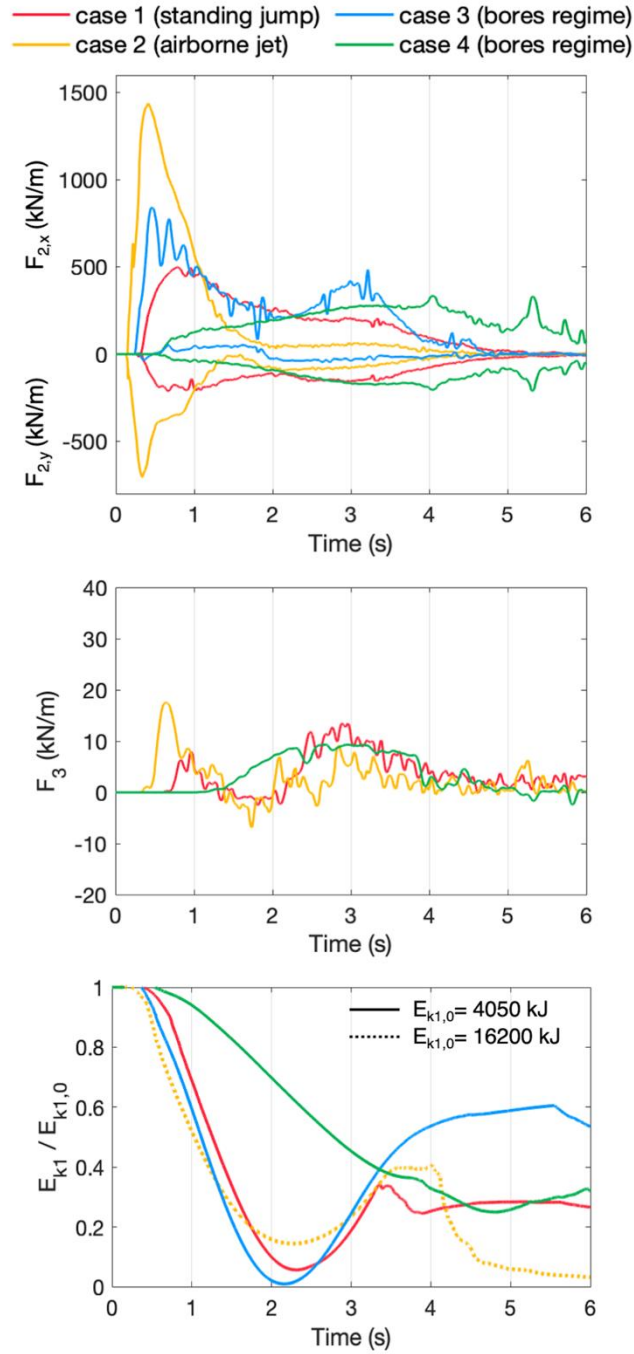


307

308

309

Figure 5. Pore-water pressure distribution for different flows:
 (a) $v_0=20$ m/s (case 2); (b) $H/h=6$ (case 4)



310

311

Figure 6. Impact forces and kinetic energy of the flow different scenarios

312

313 4 A novel empirical method

314

315 4.1 Formulation

316

317 In a simplified approach, the landslide mass is here schematized as an equivalent solid-like body,
 318 rectangular, with mass m_1 , length L_1 , depth h , unitary width, density ρ_m , initial velocity $v_{1,0}$ and it is

319 supposed to be completely stopped by the barrier (i.e., $v_1(T_2) = 0$). The latter is assumed as fixed
 320 to the base ground and indefinitely high, thus all the landslide volume is supposed to be retained by
 321 the barrier.

322 Based on the previous studies (Hung et al., 1984; Scotton and Deganutti, 1997; Kwan, 2012),
 323 the peak lateral force F_{peak} (Eq. 4) exerted by the flow on the obstacle is calculated by the sum of a
 324 dynamic component $F_{peak,dyn}$ (Fig. 7a) and a height-dependent static component $F_{peak,stat}$ (Fig. 7b),
 325 as reported in Eqs. 5-6, respectively.

326

$$327 \quad F_{peak} = F_{peak,dyn} + F_{peak,stat} \quad (4)$$

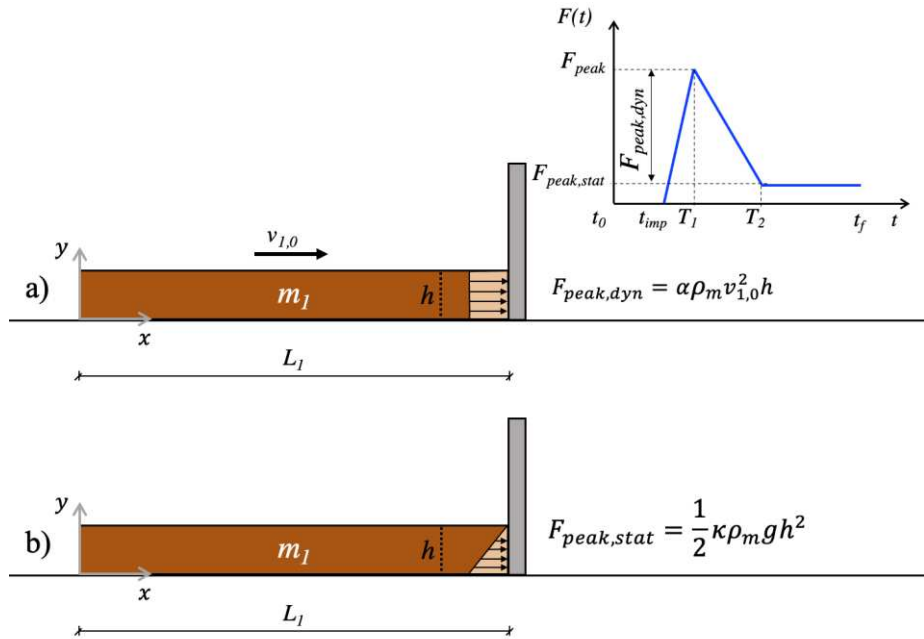
328

$$329 \quad F_{peak,dyn} = \alpha \rho_m v_{1,0}^2 h \quad (5)$$

330

$$331 \quad F_{peak,stat} = \frac{1}{2} \kappa \rho_m g h^2 \quad (6)$$

332



333

334 *Figure 7. Schematic of the impact problem in the proposed empirical model*

335

336 The empirical coefficient α has a wide range of values, ranging from 0.4 to 12 (Vagnon et al.,
 337 2020), while the empirical static coefficient κ ranges from 9 to 11 as reported by Armanini (1997) or
 338 in the range 3-30 as observed by Scheidl et al. (2013) for $Fr < 3$. This static coefficient is suggested
 339 to be assumed equal to 1 (Ng et al., 2021) for saturated flows that are fluidized due to the increasing
 340 pore pressure inside the landslide. In this paper, the value of α is calibrated based on the MPM
 341 simulation of a selected set of realistic cases.

342 The landslide kinetic energy during the impact process is derived from its velocity variation over

343 time until the impact process finishes (T_2). The impulse theorem (Eq. 7), where the impulse of the
 344 impact force is equal to the variation of linear momentum, the link between the impact pressure and
 345 velocity variation is obtained (Eq. 8). It is worth noting that the size of the impacted area (equal to h
 346 in a 2D simplification) is eliminated, being on both sides of the equation. It is implicitly assumed that
 347 the dynamic pressure is constant with the depth thus independent of h (Fig. 7a).

348 Since the time-trend of the impact pressure is a piecewise function, the equations system reads
 349 as in Eq. 9. This means that Eq. 8 is transformed into Eq. 10.

350

$$351 \quad I = \int_0^{T_2} F(t) dt = \int_{v_{1,0}}^0 m_1 dv \quad (7)$$

352

$$353 \quad \int_0^{T_2} p(t) dt = \int_{v_{1,0}}^0 m_1 dv \quad (8)$$

354

$$355 \quad p(t) = \begin{cases} \frac{p_{peak}}{T_1} t & 0 < t < T_1 \\ p_{peak} - \frac{p_{peak,dyn}}{(T_2-T_1)} (t - T_1) & T_1 < t < T_2 \end{cases} \quad (9)$$

356

$$357 \quad \int_0^{T_1} p(t) dt + \int_{T_1}^{T_2} p(t) dt = \int_{v_{1,0}}^0 m_1 dv \quad (10)$$

358

359 The reduction in landslide velocity is obtained from Eq. 11, by solving the integrals in Eq. 10 and
 360 replacing the term $p(t)$ with Eq. 9. Thus, the flow velocity over time (Eq. 12) and the corresponding
 361 kinetic energy (Eq. 13) can be computed.

362

$$363 \quad \Delta v_1(t) = \begin{cases} \frac{1}{m_1} \cdot \frac{p_{peak}}{T_1} \left(\frac{t^2}{2}\right) & 0 < t < T_1 \\ \frac{1}{m_1} \left[p_{peak}(t) - \frac{p_{peak,dyn}}{(T_2-T_1)} \left(\frac{t^2}{2}\right) \right] & T_1 < t < T_2 \end{cases} \quad (11)$$

364

365

$$366 \quad v_1(t) = v_{1,0} - \Delta v_1(t) \quad (12)$$

367

$$368 \quad E_{k,1}(t) = \frac{1}{2} m_1 v_1^2(t) \quad (13)$$

369

370 The impact period T_2 is obtained by using the impulse theorem, since the integral over time of the
 371 impact force (i.e., the impact impulse) is equal to the variation of linear momentum of the landslide
 372 (Eq. 14). The impulse of the impact force can be rewritten in terms of impact pressure, and its
 373 formulation is reported in Eq. 15. Once known T_2 through Eq. 16, T_1 can be achieved in Eq. 17 by
 374 fixing the ratio $\tau = T_1/T_2$ (for example from experimental evidence). The description of the impact

375 dynamics is complete.

376 Summing up, the model primary unknown is T_2 , while the quantities α , κ and τ , must be
377 calibrated/assessed.

378

$$379 \int_0^{T_2} F(t)dt = m_1 v_{1,0} \quad (14)$$

380

$$381 \int_0^{T_2} F(t)dt = \int_0^{T_2} p(t)hdt = \frac{1}{2}(p_{peak} + p_{peak,stat} - \tau p_{peak,stat})hT_2 \quad (15)$$

382

$$383 T_2 = \frac{2m_1 v_{1,0}}{(p_{peak} + p_{peak,stat} - \tau p_{peak,stat})h} \quad (16)$$

384

$$385 T_1 = \tau T_2 \quad (17)$$

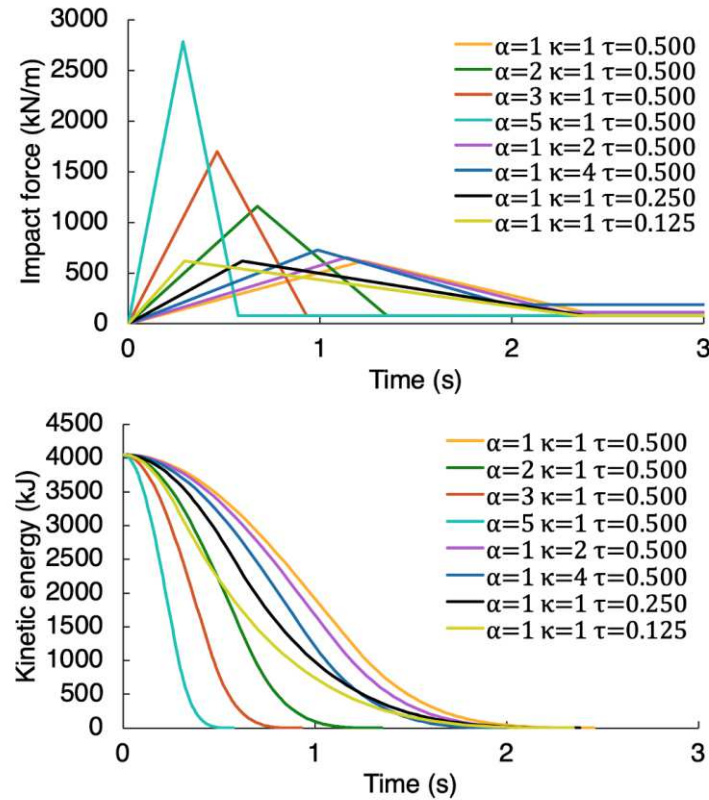
386

387 Some examples are shown in Fig. 8 to highlight the effect of α , κ and τ on impact force and kinetic
388 energy trend over time. The input quantities of the model are: $L_1 = 15 \text{ m}$; $h = 3 \text{ m}$; $\rho_m =$
389 1800 kg/m^3 ; $v_{1,0} = 10 \text{ m/s}$. High values of α result in large peak forces, short impact time T_2 and
390 rapid decrease of the kinetic energy of the flow. This means that α can be interpreted as a measure
391 of system deformability, since the decreasing of T_2 with α means that the system is more stiff.

392 The empirical coefficient κ has similar behaviour compared to α , since high values of κ result in
393 large peak forces and short time T_2 . However, the coefficient κ has a minor influence on the system
394 response compared to the coefficient α (as evident in Fig. 8); for this reason, the static component
395 of the impact force will be disregarded in this study and only the coefficient α will be used for the
396 assessment of the impact scenario.

397 Finally, the ratio τ governs the occurrence of the peak time, and thus the shape of the impact
398 force trend. In terms of flow kinetic energy dissipation, the higher the ratio τ , the steeper the
399 dissipation trend up to T_1 and the slower the energy reduction between T_1 and T_2 . In a sense, the
400 parameter τ can be interpreted as a measure of the impulsiveness of the impact loading.

401



402

403 *Figure 8. Dependence of the impact force and landslide kinetic energy on some model parameters*

404

405 4.2 Calibration

406

407 The calibration of the empirical model principally focuses on the evaluation of the empirical
408 coefficients α and τ .

409 The parameter τ is obtained by imposing the equivalence between T_1 calculated from Eq. 17, and
410 T_1 obtained from the MPM simulations.

411 The coefficient α relates to relevant features of the flow such as the grain size distribution, the
412 barrier type and the flow-structure interaction mechanism such as the formation of vertical jet-like
413 wave at the impact (Canelli et al., 2012). As reported in the literature, this parameter can vary in a
414 wide range (between 0.4 and 12), often leading to an excessive overestimation of the design impact
415 load. However, many authors (Hubl et al., 2009; Proske et al., 2011; Scheidl et al., 2013; Cui et al.,
416 2015; Vagnon, 2020) developed a power law relationship between the coefficient α and the Froude
417 number (Fr), as reported in Eq. 18.

418

$$419 \alpha = a_1 Fr^{a_2} \quad (18)$$

420

421 The evaluation of the coefficients a_1 and a_2 requires at least two numerical simulations with
422 different Froude number. Apart from cases 1, 2 and 3 of Table 1 (case 4 is neglected due to the

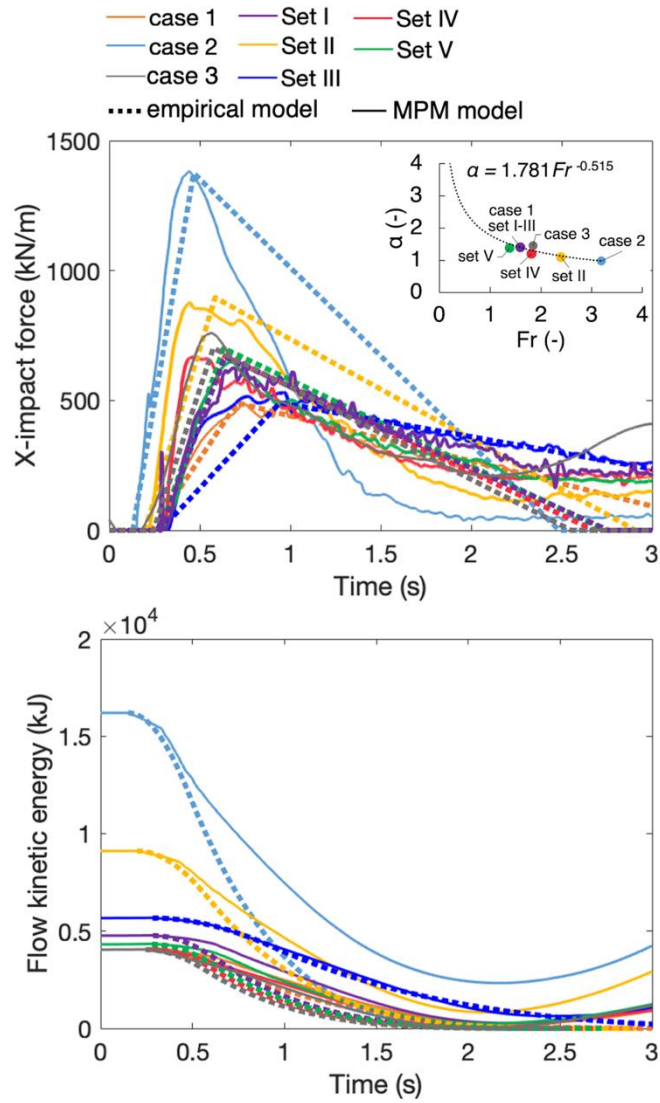
423 impossibility of identifying a unique peak value), other data-sets are used for the calibration of the
424 model (as reported in Table 4), spanning over different values of soil porosity n , flow thickness h ,
425 flow volume V_1 , initial velocity $v_{1,0}$ and the inclination β . The best fit values are $a_1 = 1.781$ and $a_2 =$
426 -0.515 (Fig. 9). The results show a good fitting with the $\alpha - Fr$ curve for all the impact scenarios,
427 and it is relevant that also the trend over time of the impact force is reproduced quite faithfully (Fig.
428 9). It entails that the peak impact pressure can be consistently obtained from the following equation:

429

$$430 \quad p_{peak} = 1.781Fr^{-0.515}\rho_m v_{1,0}^2 \quad (19)$$

431

432 Besides achieving a good correspondence with the impact forces, the trend of flow kinetic energy
433 was computed (Eq. 13) for the impact scenarios, giving for instance better agreement for the case 1
434 than the case 2. In the latter case, this is explained by the fact that high energy of the flow produces
435 a more elongated jet, which cannot be reproduced by a simplified empirical method. The flow kinetic
436 energy computed via empirical method is always lower than that computed through MPM (apart from
437 Set III). This is mostly linked to the simplifying hypothesis of neglecting the static component of the
438 impact force. However, it is a safe approximation, to be considered acceptable in the practice.



439

440 *Figure 9. Calibration of the empirical model through the MPM simulations (cases in Tables 1 and 4)*

441

442 *Table 4. Selected parameters for the calibration of the empirical model through MPM simulations*

	Flow type landslide				Barrier
	n (-)	h (m)	V_1 (m^3/m)	$v_{1,0}$ (m/s)	β ($^\circ$)
Set I	0.3	3	45 ($i = 3$)	10	60
Set II	0.5	3	45 ($i = 3$)	15	60
Set III	0.5	3	63 ($i = 5$)	10	60
Set IV	0.5	3	45 ($i = 3$)	10	80
Set V	0.5	4	48 ($i = 1$)	10	60

443

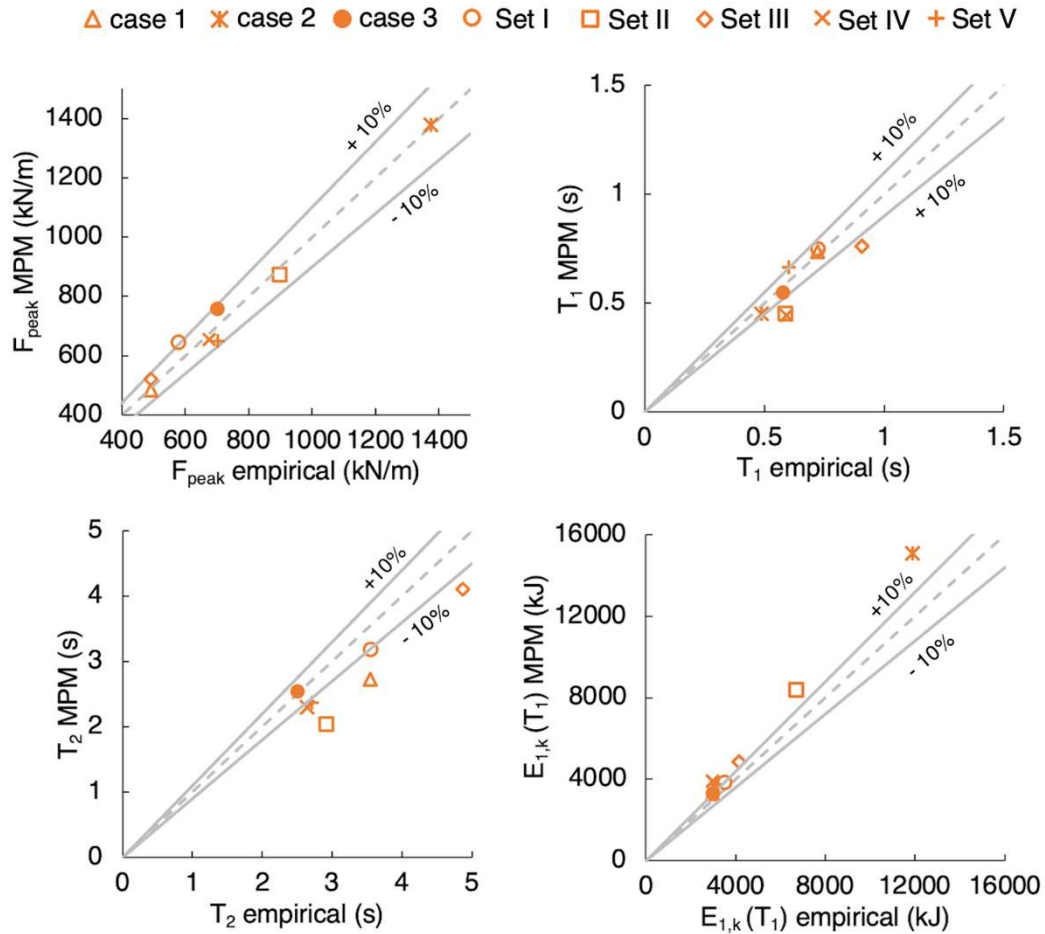
444 **4.3 Validation**

445

446 The impact scenarios used in the above-mentioned analyses are firstly used to compare the
447 output of the proposed empirical method with the numerical results for the most relevant quantities
448 in a *LSI* analysis (Fig. 10). Based on the above calibration, the values of F_{peak} and T_1 computed
449 through the empirical method (Eq. 5 and Eq. 17, respectively) fit very well the MPM numerical results
450 for all the scenarios. On the other hand, as a first validation of the method, it is observed that the
451 impact period T_2 (computed from Eq. 16) is only slightly overestimated by the empirical method
452 especially for those cases with higher velocities. In these cases, the empirical method is not able to
453 consider the amount of material which overtops the barrier. In fact, as the mass m_1 decreases, this
454 material no longer contributes to the variation of the linear momentum of the landslide (Eq. 7),
455 therefore a lower value of T_2 is expected from Eq. Only if the empirical equation is applied to the
456 condition of the indefinite wall (case 3), where the overtopping of the barrier is not allowed, then the
457 empirically-computed time T_2 perfectly matches the MPM outcome. In this case, even the other
458 calculated quantities correspond to those obtained from MPM since the indefinite wall most resemble
459 the basic assumptions of the empirical model.

460 For the evaluation of the flow kinetic energy at the peak impact force time, i.e. $E_{k,1}(T_1)$, the empirical
461 formulation provides lower values than MPM for the cases with $v_{1,0} > 10$ m/s, while there is an
462 appreciable matching for the other cases. This is mainly caused by the inability of the simplified
463 proposed method to consider the hydro-mechanical coupling and large deformations within the flow,
464 which play a crucial role during the interaction with the obstacle.

465



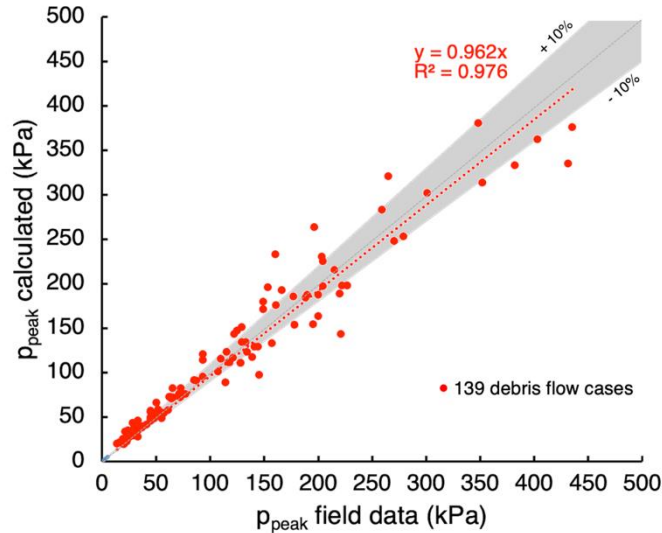
466
467 *Figure 10. Comparison of MPM and proposed empirical model*

468
469 The proposed empirical method is more thoroughly validated towards the interpretation of a large
470 dataset of real observations of flow-type landslides, achieved through a permanent monitoring
471 station. The field dataset from Hong et al. (2015) includes thickness, density, channel width, volume
472 of discharge, velocity and impact forces recorded in real time during debris flow events.

473 The data are relative to 139 historical events that took place between 1961 and 2000 in the
474 Jiangjia Ravine basin, located in the Dongchuan area of Yunnan Province in China (Zhang and
475 Xiong, 1997; Kang et al., 2007; Hong et al. 2015). The bulk density ranges from 1600 to 2300 kg/m³
476 with fluid concentration ranging from 0.15 to 0.6. The dataset is well suited for the validation purpose
477 as wide ranges of the relevant features are considered such as: $v_{1,0} = 3 - 14$ m/s, $h = 0.2 - 2.7$ m,
478 $V_1 = 269 - 1.75 \cdot 10^6$ m³ and $p_{peak} = 14 - 435$ kPa.

479 The impact pressure is calculated through the calibrated power law (Eq. 19). The results are
480 reported in Fig. 11 and show a very good correspondence with the field data, being the difference
481 much less than 10% for most of the cases. In particular, the empirical model predicts quite well the
482 peak of impact pressure for low values but showing some dispersion for values higher than 150 kPa.
483 The statistical distribution of the error, obtained as the difference between the computed value and

484 the measured value, shows that the median value is 7.18 kPa and the 90th percentile value is 36.67
485 kPa. The application of the numerical MPM model to such a large field data-set is beyond the scope
486 this paper, while it could be a future development.
487



488
489 *Figure 11. Application of the proposed empirical model to the large field dataset (139 cases)*
490 *collected by Hong et al. (2015).*

491

492 5 Discussion

493

494 A comparison between the presented methods is necessary to assess their strengths and
495 weaknesses for analyzing Landslide-Structure-Interaction.

496 MPM is an advanced numerical method and has proved to be reliable in predicting the impact
497 force trend over time (Cuomo et al., 2021). Moreover, unlike field evidence or laboratory tests, the
498 numerical results provide additional features, through the computation and time-space tracking of
499 different quantities, such as stress, strain, pore pressure, solid and liquid velocities, which cannot be
500 easily monitored or obtained in the field.

501 Particularly focusing on *LSI*, MPM has many advantages. Primarily, it allows considering all such
502 important aspects of the saturated flows, i.e. hydro-mechanical coupling and large deformations
503 during propagation and impact. The accurate knowledge of the impact mechanism and so the
504 evolution of flow depth and velocity is crucial for the design of mitigation countermeasures. For
505 example, the accurate estimate of the length of the vertical jet must prevent that the retaining
506 structure is overtopped by the flow, thus being ineffective. However, MPM suffers from some
507 limitations, such as the high computational cost and until now the difficulty of being available in
508 engineering practice.

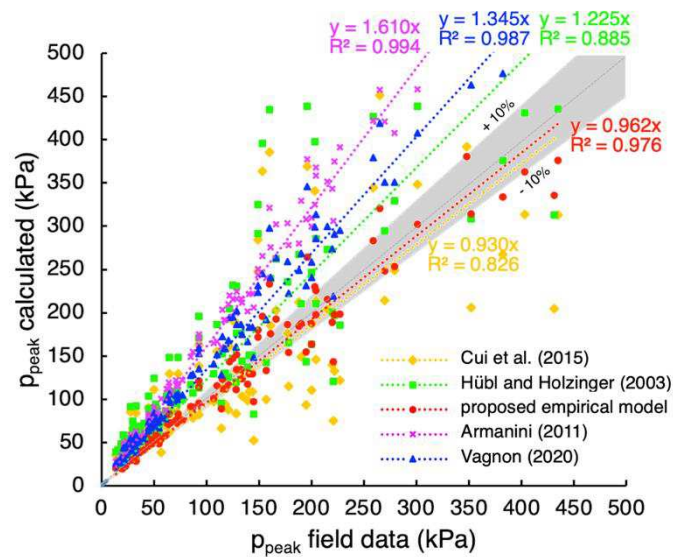
509 Empirical methods are more immediate and easier to use than MPM, since they provide an
510 estimate of the impact quantities considering only the flow density, thickness and velocity as input
511 and thus they could be preferable in the assessment of the *LSI* problems for design purposes.

512 The proposed empirical method is hence compared to some empirical formulations available in
513 the scientific literature (Fig. 12). The chosen empirical formulations are those of Hübl and Holzinger
514 (2003), Armanini et al. (2011), Cui et al. (2015) and Vagnon (2020), all included in the mixed models.

515 The large dataset used for the comparison includes 139 debris flow cases (from Hong et al. 2015)
516 already considered in paragraph 4.3. The proposed empirical model reports the highest
517 correspondence among the real data and the computed values, with a contained dispersion of the
518 results. The empirical models of Armanini et al. (2011) and Vagnon (2020) are also acceptable with
519 a low dispersion of the calculated values but with a high overestimate of 61% and 35%, respectively.
520 The formulations proposed by Hübl and Holzinger (2003) and Cui et al. (2015) are, in contrast,
521 characterized by a quite relevant variability of the achieved results.

522 Summing up all the outcomes, the MPM-based empirical model predicts very well all such
523 important quantities related to the *LSI* problem, although with some discrepancy of the results for
524 very high velocities.

525



527

527 *Figure 12. The proposed empirical method compared to some literature empirical methods*

528

529

530 **6 Conclusions**

531

532 The present paper proposed a conceptual framework and a numerical *MPM* model to analyse the
533 impact of flow-like landslides against artificial barriers, focusing not only on the evaluation of the
534 peak impact forces but also on the kinematics of the landslide during the whole impact process.

535 The conceptual framework for the Landslide-Structure-Interaction (*LSI*) problem was firstly
536 introduced to better focus the main variables that govern the dynamics of the impact process. This
537 framework has been then implemented inside the proposed methods: numerical (*MPM*) and
538 empirical.

539 Specifically, parametric *MPM* analysis has been conducted to highlight the wide range of impact
540 scenarios that can occur considering all the main features of *LSI*, such as the hydro-mechanical
541 coupling, the soil large deformations and the presence of multi-materials.

542 Then, a calibration of the new proposed empirical method was performed using the *MPM*
543 outcomes was conducted. It was possible to derive a new $\alpha - Fr$ power law relationship to derive
544 the peak impact pressure. This formulation is different from those in the literature, which are typically
545 calibrated on small-scale laboratory tests, thus giving an excessive overestimation in predicting the
546 impact load that may results in a large increment of costs for structure construction.

547 Finally, the empirical method was validated referring to a vast dataset of real field evidence
548 collected at Jiangjia Ravine (China). The achieved results are encouraging, showing a high
549 correspondence between the output of the proposed empirical formulation and the measured field
550 data. However, the estimated power law for the empirical model can lead to an underestimation of
551 peak pressures for values larger than 350 kPa, so it must be used with caution. Nevertheless, also
552 the available literature methods are applied to the same database, and thus the advantages of the
553 new method are outlined.

554 In conclusion, the models proposed in this study show a good capability to predict the impact
555 dynamics and kinematics. Further research may be directed to an enhancement of the proposed
556 empirical model considering the amount of material that can overtop the barrier, giving more accurate
557 results for the analysis of the *LSI* problem.

558

559 **7 Acknowledgments**

560

561 The research was developed within the framework of Industrial Partnership PhD Course
562 (POR Campania FSE 2014/2020). All the *MPM* simulations were performed using a version of
563 Anura3D developed by Deltares.

564

565 **Funding**

566 The research was supported by a number of Italian Research Projects funded by the Italian
567 Education and Research Ministry such as: Project FARB 2017 “Numerical modelling and inverse
568 analysis for flow-like landslides”; Project FARB 2014 “Large area analysis of triggering and
569 propagation landslide susceptibility for flow-like landslides”; Project FARB 2012 “New Frontiers of
570 advanced numerical simulation of destructive landslides”.

571 **Contributions**

572 Angela Di Perna is responsible for conceptualization, data collection and numerical modelling.
573 Sabatino Cuomo is responsible for the data collection, numerical modelling and the corresponding
574 passages in the manuscript. Mario Martinelli is responsible for numerical modelling and
575 conceptualization. The authors read and approved the final manuscript.

576

577 **Competing interests**

578 The authors declare that we have any competing financial interests.

579

580 **References**

581

582 Al-Kafaji, I. 2013. Formulation of a dynamic material point method (MPM) for geomechanical
583 problems. Ph.D. thesis, University of Stuttgart.

584 Arattano, M., & Franzi, L. J. N. H. (2003). On the evaluation of debris flows dynamics by means of
585 mathematical models. *Natural Hazards and Earth System Sciences*, 3(6), 539-544.

586 Armanini, A., Larcher, M., and Odorizzi, M. (2011). Dynamic impact of a debris flow front against a
587 vertical wall. In *Proceedings of the 5th international conference on debris-flow hazards mitigation:
588 mechanics, prediction and assessment*, Padua, Italy (pp. 1041-1049).

589 Ashwood, W., and Hungr, O. (2016). Estimating total resisting force in flexible barrier impacted by a
590 granular avalanche using physical and numerical modeling. *Canadian Geotechnical Journal*,
591 53(10), 1700-1717.

592 Bugnion, L., McArdell, B. W., Bartelt, P., and Wendeler, C. (2012). Measurements of hillslope debris
593 flow impact pressure on obstacles. *Landslides*, 9(2), 179-187.

594 Bui, H. H., & Fukagawa, R. (2013). An improved SPH method for saturated soils and its application
595 to investigate the mechanisms of embankment failure: Case of hydrostatic pore-water pressure.
596 *International Journal for numerical and analytical methods in geomechanics*, 37(1), 31-50.

597 Calvetti, F., Di Prisco, C. G., & Vairaktaris, E. (2017). DEM assessment of impact forces of dry
598 granular masses on rigid barriers. *Acta Geotechnica*, 12(1), 129-144.

599 Canelli, L., Ferrero, A. M., Migliazza, M., and Segalini, A. (2012). Debris flow risk mitigation by the
600 means of rigid and flexible barriers—experimental tests and impact analysis. *Natural Hazards and
601 Earth System Sciences*, 12(5), 1693-1699.

602 Ceccato, F., Yerro A., and Martinelli M. (2018). Modelling soil-water interaction with the Material
603 Point Method. Evaluation of single-point and double-point formulations. NUMGE, 25-29 June.
604 Porto, Portugal

605 Cui, P., Zeng, C., and Lei, Y. (2015). Experimental analysis on the impact force of viscous debris
606 flow. *Earth Surface Processes and Landforms*, 40(12), 1644-1655.

607 Cuomo, S., Prime, N., Iannone, A., Dufour, F., Cascini, L., & Darve, F. (2013). Large deformation
608 FEM-LIP drained analysis of a vertical cut. *Acta Geotechnica*, 8(2), 125-136.

609 Cuomo, S., Moretti, S., Frigo, L., Aversa, S. (2019). Deformation mechanisms of deformable
610 geosynthetics-reinforced barriers (DGRB) impacted by debris avalanches. *Bulletin of Engineering
611 Geology and the Environment*, 1-14.

612 Cuomo, S., Di Perna, A., and Martinelli, M. (2021). MPM hydro-mechanical modelling of flows
613 impacting rigid walls. *Canadian Geotechnical Journal*.

614 De Natale, J. S., Iverson, R. M., Major, J. J., LaHusen, R. G., Fiegel, G. L., and Duffy, J. D. (1999).
615 Experimental testing of flexible barriers for containment of debris flows. Reston: US Department
616 of the Interior, US Geological Survey.

617 Faug, T. 2015. Depth-averaged analytic solutions for free-surface granular flows impacting rigid walls
618 down inclines. *Physical Review E*, 92(6), 062310.

619 Fern, J., Rohe, A., Soga, K., and Alonso E. (2019). The material point method for geotechnical
620 engineering: a practical guide. CRC Press.

621 He, S., Liu, W., & Li, X. (2016). Prediction of impact force of debris flows based on distribution and
622 size of particles. *Environmental Earth Sciences*, 75(4), 298.

623 Hong, Y., Wang, J. P., Li, D. Q., Cao, Z. J., Ng, C. W. W., and Cui, P. (2015). Statistical and
624 probabilistic analyses of impact pressure and discharge of debris flow from 139 events during
625 1961 and 2000 at Jiangjia Ravine, China. *Engineering Geology*, 187, 122-134.

626 Hübl, J., Suda, J., Proske, D., Kaitna, R., and Scheidl, C. (2009). Debris flow impact estimation. In
627 Proceedings of the 11th international symposium on water management and hydraulic
628 engineering, Ohrid, Macedonia (Vol. 1, pp. 1-5).

629 Hungr, O., Morgan, G. C., and Kellerhals, R. (1984). Quantitative analysis of debris torrent hazards
630 for design of remedial measures. *Canadian Geotechnical Journal*, 21(4), 663-677.

631 Idelsohn, S. R., Oñate, E., and Pin, F. D. (2004). The particle finite element method: a powerful tool
632 to solve incompressible flows with free-surfaces and breaking waves. *International journal for
633 numerical methods in engineering*, 61(7), 964-989.

634 Iverson, R. M. (1997). The physics of debris flows. *Reviews of geophysics*, 35(3), 245-296.

635 Li, X., Zhao, J., & Soga, K. (2021). A new physically based impact model for debris flow.
636 *Géotechnique*, 71(8), 674-685.

637 Jassim, I., Stolle, D., and Vermeer, P. (2013). Two-phase dynamic analysis by material point
638 method. *International journal for numerical and analytical methods in geomechanics*, 37(15),
639 2502-2522.

640 Jeong, S., & Lee, K. (2019). Analysis of the impact force of debris flows on a check dam by using a
641 coupled Eulerian-Lagrangian (CEL) method. *Computers and Geotechnics*, 116, 103214.

642 Kang, Z. C., Cui, P., Wei, F. Q., and He, S. F. (2007). Data collection of observation of debris flows
643 in Jiangjia Ravine, Dongchuan Debris Flow Observation and Research Station (1995-2000).

644 Kwan, JSH. (2012). Supplementary technical guidance on design of rigid debris-resisting barriers.
645 GEO Report No. 270, Geotechnical Engineering Office, Civil Engineering and Development
646 Department, Hong Kong SAR Government.

647 Leonardi, A., Wittel, F. K., Mendoza, M., Vetter, R., & Herrmann, H. J. (2016). Particle–fluid–structure
648 interaction for debris flow impact on flexible barriers. *Computer-Aided Civil and Infrastructure*
649 *Engineering*, 31(5), 323-333.

650 Luo, H., Baum, J. D., and Löhner, R. 2008. A discontinuous Galerkin method based on a Taylor
651 basis for the compressible flows on arbitrary grids. *Journal of Computational Physics*, 227(20),
652 8875-8893.

653 Mast, C. M., Mackenzie-Helnwein, P., Arduino, P., Miller, G.R. and Shin W. (2012). Mitigating
654 kinematic locking in the material point method. *Journal of Computational Physics*, 231(16), 5351–
655 5373.

656 Mieremet, M. M. J., Stolle, D. F., Ceccato, F., and Vuik, C. 2016. Numerical stability for modelling of
657 dynamic two-phase interaction. *International Journal for Numerical and Analytical Methods in*
658 *Geomechanics*, 40(9), 1284-1294.

659 Ng, C. W. W., Majeed, U., Choi, C. E., and De Silva, W. A. R. K. (2021). New impact equation using
660 barrier Froude number for the design of dual rigid barriers against debris flows. *Landslides*, 1-13.

661 Proske, D., Suda, J., and Hübl, J. (2011). Debris flow impact estimation for breakers. *Georisk*, 5(2),
662 143-155.

663 Qiu, G., Henke, S., & Grabe, J. (2011). Application of a Coupled Eulerian–Lagrangian approach on
664 geomechanical problems involving large deformations. *Computers and Geotechnics*, 38(1), 30-
665 39.

666 Scheidl, C., Chiari, M., Kaitna, R., Müllegger, M., Krawtschuk, A., Zimmermann, T., and Proske, D.
667 (2013). Analysing debris-flow impact models, based on a small scale modelling approach.
668 *Surveys in Geophysics*, 34(1), 121-140.

669 Scotton, P., and Deganutti, A.M. (1997). Phreatic Line and Dynamic Impact in Laboratory Debris
670 Flow Experiments.

671 Shen, W., Zhao, T., Zhao, J., Dai, F., & Zhou, G. G. (2018). Quantifying the impact of dry debris flow
672 against a rigid barrier by DEM analyses. *Engineering Geology*, 241, 86-96.

673 Song, D., Ng, C. W. W., Choi, C. E., Zhou, G. G., Kwan, J. S., and Koo, R. C. H. 2017. Influence of
674 debris flow solid fraction on rigid barrier impact. *Canadian geotechnical journal*, 54(10), 1421-
675 1434.

676 Song, D., Zhou, G. G., Chen, X. Q., Li, J., Wang, A., Peng, P., & Xue, K. X. (2021). General equations
677 for landslide-debris impact and their application to debris-flow flexible barrier. *Engineering*
678 *Geology*, 288, 106154.

679 Thouret, J. C., Antoine, S., Magill, C., and Ollier, C. (2020). Lahars and debris flows: Characteristics
680 and impacts. *Earth-Science Reviews*, 201, 103003.

- 681 Vagnon, F. (2020). Design of active debris flow mitigation measures: A comprehensive analysis of
682 existing impact models. *Landslides*, 17(2), 313-333.
- 683 Vagnon, F., and Segalini, A. (2016). Debris flow impact estimation on a rigid barrier. *Natural Hazards
684 and Earth System Sciences*, 16(7), 1691-1697.
- 685 Zhang, J., and Xiong, G. (1997). Data collection of kinematic observation of debris flows in Jiangjia
686 Ravine, Dongchuan, Yunnan (1987-1994).
- 687 Zhou, G. G. D., Song, D., Choi, C. E., Pasuto, A., Sun, Q. C., and Dai, D. F. (2018). Surge impact
688 behavior of granular flows: effects of water content. *Landslides*, 15(4), 695-709.

689 **Appendix 1. Material Point Method model equations**

690

691 The Material Point Method (MPM) is an enhancement of the Finite Element Method (FEM), and
692 it is very well suited for large deformation problems. The continuum body consists of several
693 Lagrangian points (named material points, MPs), which carry all the physical properties of the
694 continuum such as stress, strain, density, momentum, material parameters and other state
695 parameters. The MPs move across a background mesh, which covers the domain where the material
696 is expected to move, and it is used to solve the governing equations without storing any permanent
697 information.

698 A saturated porous medium is schematized as a solid phase which represents the solid skeleton,
699 whereas the liquid phase fills the voids among the grains. Each MP represents a volume of the
700 mixture V , given by the sum of the solid V_S and liquid V_L phases volumes. The behaviour of a
701 saturated porous medium is here described using only one set of MPs, in which the information
702 about both the solid and liquid constituents is stored. The interaction between phases (solid and
703 liquid in a saturated soil) can be tackled through the *two-phase single-point* formulation (Jassim et
704 al., 2013; Ceccato et al., 2018), where the liquid and the solid acceleration fields ($\mathbf{a}_S - \mathbf{a}_L$ formulation)
705 are the primary unknowns (Fern et al., 2019).

706 The velocity field of solid and liquid phases are both used, but the material points move
707 throughout the mesh with the kinematics of the solid skeleton. The equations to be solved concern
708 the balance of dynamic momentum of solid and liquid phases, the mass balances, and the
709 constitutive relationships of solid and liquid phases. The accelerations of the two phases are the
710 primary unknowns: the solid acceleration \mathbf{a}_S , which is calculated from the dynamic momentum
711 balance of the solid phase (Eq. A1), and the liquid acceleration \mathbf{a}_L , which is obtained by solving the
712 dynamic momentum balance of the liquid phase (Eq. A2). The interaction force between solid and
713 liquid phases is governed by Darcy's law (Eq. A3). Numerically, these equations are solved at grid
714 nodes considering the Galerkin method (Luo et al., 2008) with standard nodal shape functions and
715 their solutions are used to update the MPs velocities and momentum of each phase. The strain rate
716 $\dot{\epsilon}$ of MPs is computed from the nodal velocities obtained from the nodal momentum.

717

$$718 \quad n_S \rho_S \mathbf{a}_S = \nabla \cdot (\boldsymbol{\sigma} - n p_L \mathbf{I}) + (\rho_m - n \rho_L) \mathbf{b} + \mathbf{f}_d \quad (\text{A1})$$

719

$$720 \quad \rho_L \mathbf{a}_L = \nabla p_L - \mathbf{f}_d \quad (\text{A2})$$

721

$$722 \quad \mathbf{f}_d = \frac{n \mu_L}{k} (\mathbf{v}_L - \mathbf{v}_S) \quad (\text{A3})$$

723

724 The resolution of solid and liquid constitutive laws (Eqs. A4-A5) allows calculating the increment
 725 of effective stress $d\boldsymbol{\sigma}'$ and excess pore pressure dp_L , respectively. The mass balance equation of
 726 the solid skeleton is then used to update the porosity of each MP (Eq. A6), while the total mass
 727 balance serves to compute the volumetric strain rate of the liquid phase (Eq. A7) since fluxes due to
 728 spatial variations of liquid mass are neglected ($\nabla n \rho_L = 0$).

729

$$730 \quad d\boldsymbol{\sigma}' = \mathbf{D} \cdot d\boldsymbol{\varepsilon} \quad (\text{A4})$$

731

$$732 \quad dp_L = \mathbf{K}_L \cdot d\varepsilon_{vol} \quad (\text{A5})$$

733

$$734 \quad \frac{Dn}{Dt} = n_S \nabla \cdot \mathbf{v}_S = \mathbf{0} \quad (\text{A6})$$

735

$$736 \quad \frac{D\varepsilon_{vol}}{Dt} = \frac{n_S}{n} \nabla \cdot \mathbf{v}_S + \nabla \cdot \mathbf{v}_L \quad (\text{A7})$$

737

738 In the two-phase single-point formulation the liquid mass, and consequently the mass of the
 739 mixture, is not constant in each material point but can vary depending on porosity changes. Fluxes
 740 due to spatial variations of liquid mass are neglected and Darcy's law is used to model solid-liquid
 741 interaction forces. For this reason, this formulation is generally used in problems with small gradients
 742 of porosity, and laminar and stationary flow in slow velocity regime. However, this formulation proves
 743 to be suitable for studying flow-structured-interaction (Cuomo et al., 2021). The water is assumed
 744 linearly compressible via the bulk modulus of the fluid \mathbf{K}_L and shear stresses in the liquid phase are
 745 neglected.

746 The current MPM code uses 3-node elements which suffer kinematic locking, which consists in
 747 the build-up of fictitious stiffness due to the inability to reproduce the correct deformation field (Mast
 748 et al., 2012). A technique used to mitigate volumetric locking is the strain smoothing technique,
 749 which consists of smoothing the volumetric strains over neighbouring cells. The reader can refer to
 750 Al-Kafaji (2013) for a detailed description.

751 Regarding the critical time step, the influence of permeability and liquid bulk modulus must be
 752 considered as well (Mieremet et al., 2016). In particular, the time step required for numerical stability
 753 is smaller in soil with lower permeability (Eq. A8).

754
$$\Delta t_{cr} = \min \left(\frac{d}{\sqrt{(E+K_L/n)/\rho_m}}; \frac{2(\rho_m+(1/n-2)\rho_L)k_{sat}}{\rho_L g} \right) \quad (A8)$$

755

756

757 The sliding modelling of the flowing mass on the rigid material is handled by a frictional Mohr-
 758 Coulomb strength criterion. The contact formulation was used to ensure that no interpenetration
 759 occurs, and the tangential forces are compatible with the shear strength along the contact. The
 760 reaction force acting on the structure at node j was calculated as in Eq. A9.

761

762
$$F_j(t) = m_{j,S}\Delta a_{S,contact} + m_{j,L}\Delta a_{L,contact} \quad (A9)$$

763

764 The terms $\Delta a_{S,contact}$ and $\Delta a_{L,contact}$ are the change in acceleration induced by the contact
 765 formulation, for both solid and liquid phase, and $m_{i,S}$ and $m_{i,L}$ are the corresponding nodal masses.
 766 The total reaction force is the integral of the nodal reaction forces along the barrier.

767